

Study of Transport Phenomena in Chromatographic Columns by Pulsed Field Gradient NMR

Ulrich Tallarek,^{†,‡} Dagmar van Dusschoten,[‡] Henk Van As,[‡] Ernst Bayer,[†] and Georges Guiochon^{*,§}

Institute of Organic Chemistry, University of Tübingen, Auf der Morgenstelle 18, 72076 Tübingen, Germany, Department of Molecular Physics, Wageningen Agricultural University, and Wageningen NMR Center, Dreijenlaan 3, 6703 HA Wageningen, The Netherlands, Department of Chemistry, University of Tennessee, Knoxville, Tennessee, 37996-1600, and Chemical and Analytical Sciences Division, Oak Ridge National Laboratory, Oak Ridge, Tennessee 37831

Received: November 18, 1997; In Final Form: February 24, 1998

Pulsed field gradient NMR has been applied to study mass transfer, flow, and dispersion in packed chromatographic columns. A single measurement allows the determination of the full displacement probability distribution of all fluid particles located in the measurement volume. Depending on the orientation of the pulsed magnetic field gradient with respect to the net flow direction, the so-called averaged propagator is obtained independently and quantitatively for either the axial or the transverse fluid particle displacements, over an experimentally adjustable observation time. Thus, this technique can act on a dynamic time scale ranging from a few to several hundred milliseconds. This enabled us to detect the stagnant mobile phase in packed chromatographic columns and to follow the mass transfer between the stagnant solvent and the stream of mobile phase percolating through the column bed. With field gradients in the direction of net flow velocity, mean fluid particle displacements ranging between 0.07 and 100 times the average diameter of the stationary phase particles could be analyzed in terms of the intimately associated averaged propagator, with observation times between 30 and 960 ms. Starting in the absence of flow, the development from the Gaussian propagator for molecular diffusion in the packing (centered at zero net displacement) toward the fully established Gaussian propagator (parallel to the onset and increase of externally driven flow) is recorded, characterizing convection-driven dispersion in the packing. For short observation times, the mass transfer between the deep pools of stagnant mobile phase in the totally porous support particles and the interstitial space in the packed bed is found to be incomplete and the transition toward complete exchange is followed. The results indicate that the stagnant mobile-phase mass transfer in the classical HPLC silica-based stationary phase is purely diffusion-controlled.

Introduction

Rate limitations due to the diffusional mass transfer through the stagnant mobile phase impregnating porous particles have long been recognized as a major source of axial dispersion in adsorption and ion-exchange chromatography.^{1–6} This contribution to the overall mass-transfer resistances is especially important in the development of fast separations and in the purification of slowly diffusing macromolecules (e.g., proteins).⁷ In such cases, separations are carried out in a range of velocities well above the minimum of the classical van Deemter curve,^{8,9} which correspond to values of the Peclet number or reduced velocity ($Pe = v = \bar{u} d_p/D_m$) exceeding 3–5, where Pe is the Peclet number, v is the reduced velocity, \bar{u} is the cross-sectional average velocity of the mobile phase, d_p is the average particle size, and D_m is the diffusivity of the solute studied. Thus, this contribution to mass-transfer resistance is intimately related to the size, shape, and internal architecture (pore size distribution, pore shape, pore connectivity) of the particles of the porous packing material, i.e., to the mechanisms governing mass transfer within the tortuous pore network of a single particle.

Several solutions have been proposed to reduce the importance of the intraparticle mass-transfer resistance, such as the use of small totally porous particles in HPLC^{10,11} (see Figure 1) and—to the expense of the specific surface area available for retention—even the use of nonporous particles.¹² The resistance to mass transfer through the stagnant mobile phase was also found to be dramatically reduced with superficially porous beads as compared to totally porous particles of the same size.¹³ Porous particles of 2–5 μm in diameter are commonly used now for analytical applications. Further reduction of the particle size is limited by practical considerations, the column permeability decreasing rapidly with decreasing average particle size. Porous particles of 10–30 μm in diameter are more commonly used in preparative chromatography. Although small nonporous and superficially porous particles are available and provide high-efficiency columns, their use is limited by the drawback of a severely limited sample capacity.

These different routes have in common the minimization (or even the elimination) of slow diffusion steps inside the porous particles. The overall design of the particle was seen to be of crucial importance in achieving this goal, maintaining broad chromatographic practicability at the same time.⁵ Considerable research and development work has been dedicated to the

[†] University of Tübingen.

[‡] Wageningen Agricultural University and Wageningen NMR Center.

[§] University of Tennessee and Oak Ridge National Laboratory.

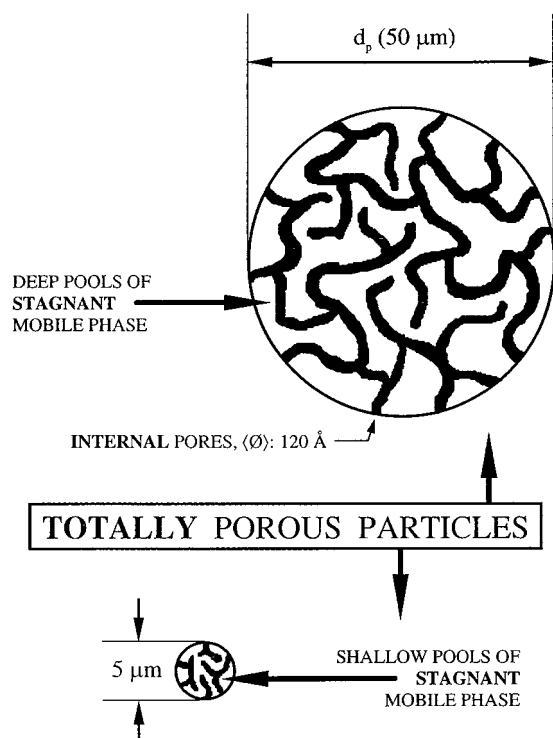


Figure 1. Stagnant mobile phase in large and small totally porous, purely diffusive adsorbent particles typically used for HPLC applications.

preparation of silica gel particles with a pore network causing minimum hindrance to diffusional transfer.¹⁴ The importance of pore connectivity has been recognized.¹⁵ The most significant recent conceptual improvement in this area, perfusion chromatography, was recognized long ago in gel permeation chromatography.¹⁶ It requires particles having large flow-through pores and allows high-speed separations of (bio)macromolecules.¹⁷ By incorporation of large particle transecting pores (flow-through pores) into the network of smaller (diffusive) pores, the resulting interconnected bimodal pore network (a) minimizes the diffusion path lengths in the highly porous particle and (b) enables convective transport in the through-pores. This intraparticle convection effectively assists the transport of solute molecules to the active sites in the interior of the porous adsorbent particles and (at high mobile-phase velocities) dominates over the classical (diffusional) stagnant mobile-phase mass transfer.¹⁸

Further progress in this area requires a better understanding of the nature of the fluid dynamic properties in beds of porous particles and the systematic measurement of the corresponding parameters. The results of such investigations would have important consequences for the development and optimization of packing materials for analytical and preparative scale liquid chromatography. This requirement, in turn, necessitates the use of techniques capable of providing profound insights into the transport phenomena in the beds of packed columns and acting on a time scale sufficient directly to follow mass transfer through and exchange between phases. Pulsed field gradient (PFG) NMR is such a technique.¹⁹ It allows the direct detection and visualization of the stagnant mobile phase in a liquid chromatographic column and the study of the associated exchange between the respective stagnant and net moving volume fractions of a single fluid phase, under conditions of externally driven convection. The aim of this report is to present the results of a first investigation of the mass-transfer kinetics in a packed column by PFGNMR.

Previously, this technique has been used to study the flow velocity distributions in an unconsolidated bed of nonporous glass beads²⁰ ($d_p = 800 \pm 150 \mu\text{m}$) fitted inside a conventional 8-mm i.d. NMR glass tube or to investigate fluid transport in solid rocks like cylindrical samples of Bentheimer²¹ and Fontainebleau sandstones.^{22,23} In most of these works, attention was focused on displacements of the fluid particles much smaller than the typical pore size, at flow rates high enough that the influence of molecular diffusivity could be neglected. In such cases, PFGNMR provided a detailed velocity distribution of the fluid in the interparticle pore network. An exponential decay was found for the probability distribution of the higher velocity components, being in good agreement with the results of calculations in which the Stokes equation was solved directly in the geometry of a random packing of spheres constructed numerically.²⁰

In this work, we used classical chromatographic packing materials, made of fine porous silica particles, well-consolidated packings. Mass-transfer resistances become evident at short observation times, at which an incomplete exchange between the flowing and the stagnant fractions of the fluid phase can be detected. These noninvasive measurements utilize the direct Fourier relationship between the recorded NMR signal and the so-called "averaged propagator", a quantity that simply describes the probability for any dynamic displacement of the fluid molecules.²⁴ The net displacement of any fluid particle within the measurement volume is captured to contribute its weight to the displacement probability distribution, irrespective of its location (e.g., in the stagnant or the flowing liquid phase) and of its dynamic course over the observation time (i.e., exchange between environments having different dynamic properties). Quantitative displacement profiles are inherently related to the observation time scale chosen in the PFGNMR experiment. They are obtained independently for axial and for transverse particle displacements.

Thus, PFGNMR measurements provide a direct determination of the range and weight of the net displacements of the molecules of the fluid phase in the column bed. These displacements are related to experimental parameters that can be controlled easily and accurately, namely, the fluid flow rate, the observation time (between 30 and 960 ms), and the direction of the magnetic field gradient (axial or transverse). By independently changing the volume flow rate of the mobile phase and the observation time of the experiment, the technique allows the determination of the kinetics of mass transfer between diffusion-limited regions of the packed column and (net) flowing parts, at constant flow rate. It also allows the study of the transition from purely diffusion-driven dispersion (without flow) to classical convection-driven dispersion in the porous packing, at constant observation time, by simply changing the flow rate, i.e., by increasing the ratio of the migration path lengths to the particle diameter.

Physical Considerations

The averaged propagator, $\bar{P}(\mathbf{R}, \Delta)$, obtained by PFGNMR for the fluid in the column, gives the probability that any fluid molecule (independently of its starting positions, \mathbf{r}_0) will undergo a dynamic (i.e., net) displacement $\mathbf{R} = \mathbf{r} - \mathbf{r}_0$ along the direction of the applied pulsed field gradients within the experimentally adjustable (and well-defined) observation time, Δ .^{24,25} Thus, $\bar{P}(\mathbf{R}, \Delta)$ is the spatial average of $P(\mathbf{r}/\mathbf{r}_0, \Delta)$, the conditional probability that describes the likelihood that a molecule originally located at \mathbf{r}_0 will have migrated to \mathbf{r} over time Δ .

$$\bar{P}(\mathbf{R}, \Delta) = \int \rho(\mathbf{r}_0) P(\mathbf{r}/\mathbf{r}_0, \Delta) d\mathbf{r}_0 \quad (1)$$

where $\rho(\mathbf{r}_0)$ is the normalized density of the initial spin positions (and also of the fluid particles that intrinsically carry the nuclear spins, i.e., the molecules $^1\text{H}_2\text{O}$).

Applying the pulsed field gradients in a direction either parallel or perpendicular to the column axis allows the independent determination of the axial or the transverse averaged propagator, respectively. This propagator is obtained on the basis of its Fourier relation with the echo amplitude, $E(\mathbf{g}, \delta, \Delta)$. In this Fourier sense, $\bar{P}(\mathbf{R}, \Delta)$ and $E(\mathbf{g}, \delta, \Delta)$ are conjugated²⁶

$$E(\mathbf{g}, \delta, \Delta) = \frac{S(\mathbf{g}, \delta, \Delta)}{S(0, \delta, \Delta)} = \int \bar{P}(\mathbf{R}, \Delta) \exp(i\gamma\delta\mathbf{g}\cdot\mathbf{R}) d\mathbf{R} \quad (2)$$

where $E(\mathbf{g}, \delta, \Delta)$ represents the normalized echo amplitude in an ideal PFGNMR experiment with gradient pulses of amplitude (and direction) \mathbf{g} and duration δ , a time that must be sufficiently narrow that we can neglect the motion of spins over their duration.²⁷ $S(0, \delta, \Delta)$ represents the echo signal measured in the absence of externally applied field gradients. The gradient area defines the so-called \mathbf{q} -space vector, $\mathbf{q} = \gamma\delta\mathbf{g}/(2\pi)$.²⁸ This space is the reciprocal of the dynamic displacement space, \mathbf{R} . Consequently, eq 2 can be expressed as¹⁹

$$E(\mathbf{q}, \Delta) = \frac{S(\mathbf{q}, \Delta)}{S(0, \Delta)} = \int \bar{P}(\mathbf{R}, \Delta) \exp(i2\pi\mathbf{q}\cdot\mathbf{R}) d\mathbf{R} \quad (3)$$

It should be pointed out that this formalism is entirely analogous to that for the coordinate space in conventional NMR microscopy. In that case, the imaging gradient (of amplitude and direction \mathbf{G} and duration t) defines the so-called \mathbf{k} -space vector, $\mathbf{k} = \gamma\mathbf{G}t/(2\pi)$. This space is the conjugate of the space of static displacement, \mathbf{r} . For \mathbf{k} -space imaging, the spin density, $\rho(\mathbf{r})$, is then obtained by Fourier transform of the detected signal, $S(\mathbf{k})$, with respect to \mathbf{k} :

$$S(\mathbf{k}) = \int \rho(\mathbf{r}) \exp(i2\pi\mathbf{k}\cdot\mathbf{r}) d\mathbf{r} \quad (4)$$

For effective dispersion of the fluid particles in the column bed, the averaged propagator distribution is *Gaussian*, being intimately related to the axial or transverse dispersion event over time, Δ

$$\bar{P}(\mathbf{R}, \Delta) = \frac{1}{\sqrt{2\pi\sigma^2}} \exp\left(-\frac{\mathbf{R}^2}{2\sigma^2}\right) \quad (5)$$

where $\sigma^2 = 2D_{\text{ap}}\Delta$ is the averaged mean-square displacement of spins during the time interval Δ , measured in the direction of the applied pulsed field gradients, and D_{ap} is the apparent (axial, $D_{\text{ap,a}}$, or transverse, $D_{\text{ap,t}}$) dispersion coefficient in the medium. Incorporating the effect of net flow²⁹ with a cross-sectional average velocity $\bar{\mathbf{u}}$ superimposed on the dispersion, one finally arrives at

$$\bar{P}(\mathbf{R}, \Delta) = \frac{1}{\sqrt{4\pi D_{\text{ap}}\Delta}} \exp\left(-\frac{(\mathbf{R} - \bar{\mathbf{u}}\Delta)^2}{4D_{\text{ap}}\Delta}\right) \quad (6)$$

With this expression for the averaged propagator, $E(\mathbf{q}, \Delta)$ takes on the form of an oscillatory function of \mathbf{q} , depending on the gradient orientation (\mathbf{g}) with respect to the flow direction ($\bar{\mathbf{u}}$) and is modulated by a Gaussian decay envelope. Then, the complex \mathbf{q} -space Fourier transform, $\mathbf{F}\{E(\mathbf{q}, \Delta)\}$, corresponds

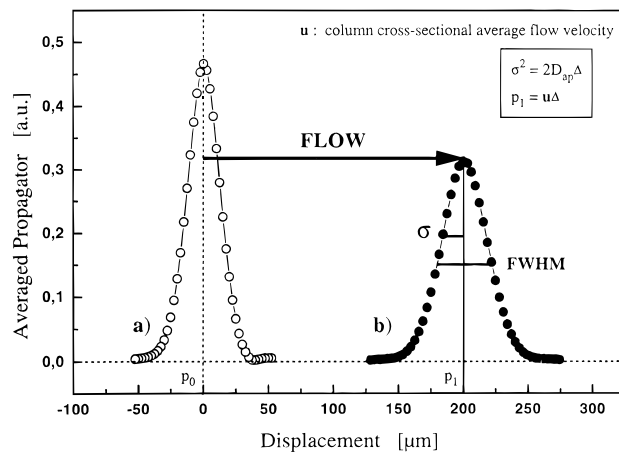


Figure 2. Effect of externally driven convection and observation time Δ of the experiment on shape and position of displacement probability (averaged propagator) distributions measured by PFGNMR (b). The apparent axial dispersion coefficient D_{ap} and cross-sectional average velocity $\bar{\mathbf{u}}$ can be calculated from the standard deviation and center position of the Gaussian distribution, respectively. In the absence of flow and also when measured in the transverse direction, $\bar{P}(\mathbf{R}, \Delta)$ is centered at zero net displacement (a).

to a Gaussian curve of standard deviation $(2D_{\text{ap}}\Delta)^{1/2}$, centered at $\bar{\mathbf{u}}\Delta$ in the displacement space:

$$E(\mathbf{q}, \Delta) = \exp[-4\pi\mathbf{q}^2 D_{\text{ap}}\Delta + i2\pi\mathbf{q}\bar{\mathbf{u}}\Delta] \quad (7)$$

$$\mathbf{F}|E(\mathbf{q}, \Delta)| = \frac{1}{\sqrt{4\pi D_{\text{ap}}\Delta}} \exp\left(-\frac{\mathbf{R}^2}{4D_{\text{ap}}\Delta}\right) \otimes \delta(\mathbf{R} - \bar{\mathbf{u}}\Delta) \quad (8)$$

Finally, the convolution with the δ -function determines the position of the Gaussian curve along the displacement axis. So, the cross-sectional average velocity $\bar{\mathbf{u}}$ and the apparent dispersion coefficient D_{ap} can be extracted from the profile peak center and the profile width, respectively (see Figure 2). Thus, for $\bar{P}(\mathbf{R}, \Delta)$ measured in the transverse direction (with $\mathbf{g}, \mathbf{q} \perp \bar{\mathbf{u}}$), the displacement probability distributions are centered at zero displacement (because there is no net flow in this direction), whereas in the axial direction (for which $\mathbf{g}, \mathbf{q} \parallel \bar{\mathbf{u}}$), the averaged propagator distribution is shifted to finite displacements, according to the dynamic parameter $\bar{\mathbf{u}}\Delta$.

This fact also allows an accurate estimate of the total porosity of the bed accessible to the mobile phase which is obtained from the center position of the Gaussian displacement probability distribution curves (at $\bar{\mathbf{u}}\Delta$), by means of the classical relationship

$$\nu = \frac{\bar{\mathbf{u}}d_p}{D_m} = \frac{4F_v d_p}{\epsilon_T \pi d_c^2 D_m} \quad (9)$$

with ν , the reduced flow velocity (or particle Peclet number), F_v , the volume flow rate of the mobile phase, d_p , the average particle size, D_m , the molecular diffusivity of the bulk mobile phase, $\bar{\mathbf{u}}$, the cross-sectional average velocity, ϵ_T , the total porosity of the bed, and d_c , the column diameter. All parameters but ϵ_T in this relationship are known or measured independently.

The total porosity, i.e., the volume fraction occupied by the mobile phase in the column, includes the volume fraction occupied by the pores inside the particles (internal porosity) as well as the volume fraction of the voids between and around the packed particles (external porosity). Using this new approach, the best estimates of the total mobile phase porosities (ϵ_T) of the packed beds used in this study are: 0.73 for the 16

mm i.d. glass column packed with the totally porous, spherical shaped, neat silica particles ($d_p = 50 \mu\text{m}$); 0.67 for the 4.4 mm i.d. PEEK column packed with totally porous, chemically bonded C18 silica particles ($d_p = 50 \mu\text{m}$); and 0.65 for the 4.4 mm i.d. PEEK column packed with the totally porous C18 silica particles of $15 \mu\text{m}$ average diameter.

Experimental Section

The columns used in this study were made of either PEEK (poly(arylether ether ketone), $4.4 \times 150 \text{ mm}$) or glass, the latter being a Merck Superformance axial compression system ($16 \times 300 \text{ mm}$; Merck, Darmstadt, Germany). Packing materials used were made of totally porous silica particles, either chemically bonded C18 or native, spherical in shape, with average particle diameters of 15 and $50 \mu\text{m}$, respectively (YMC Europe, Schermbeck, Germany). The columns were slurry-packed.³⁰ An approximately 5% slurry of the packing material in degassed 2-propanol was forced into the column using a hydropneumatic HPLC pump (Knauer, Berlin, Germany), with degassed methanol as the pushing solvent. After the column tube was filled, the inlet pressure was raised to consolidate the packing material under the viscous stress caused by the fast solvent stream. All solvents were thoroughly degassed. For the 4.4 mm i.d., 150 mm long PEEK columns, the consolidation pressure was adjusted to 250 atm (for ca. 35 min); in the case of the glass column (16 mm i.d. and jacket length of 300 mm), it was limited to 80 atm (ca. 60 min). The PEEK columns were closed with UHMWPE or PEEK frits (Upchurch Scientific, Oak Harbor, WA). The PEEK unions, fingertights, and column end fittings were manufactured out of PEEK rods in the workshop of the University of Tübingen. Finally, the columns were directly inserted into the radio-frequency (rf) and gradient coil system in the magnet.

One of the practical advantages of PFGNMR is that no sample has to be injected into the column. The experiment design uses the liquid phase itself as the probe of fluid particle displacements. So, no injection valves nor detectors were needed. Pure, degassed water was simply pumped continuously through the column bed under study. A conventional analytical pump head was adapted to a Sykam pump (model S 1000; Sykam, Gilching, Germany) for flow rates up to 11 mL/min. The actual volume flow rate, F_v , was determined by measuring the volume of effluent collected during a given time. The pump was placed about 1.5 m away from the magnet.

The ^1H PFGNMR measurements were performed at $23 \pm 0.5^\circ\text{C}$ on a Bruker 0.5 T electromagnet with power supply (Bruker, Karlsruhe, Germany), operating at 0.478 T (corresponding to 20.35 MHz for the ^1H nucleus). Magnetic field gradients were applied to the sample using a special, custom-built microscopy probe from Doty Scientific (Columbia, OH), with actively shielded gradients. They are driven by a single-channel Techtron 7570 and a Crown DG-300A dual-channel amplifier (Analogue Associates Ltd., Norfolk, England). The two gradient drivers and a 1 kW AN 8031 rf amplifier (Analogic, Wakefield, MA) are controlled by a S.M.I.S. console (Surrey Medical Imaging Systems, Guildford, England). In the direction parallel to the column axis (i.e., perpendicular to the direction of the main magnetic field, B_0), gradient amplitudes of up to 500 mT/m can be used. In the direction perpendicular to the column axis (i.e., parallel to B_0), the maximum attainable gradient strength is 600 mT/m.

In our experiments, we adopted the stimulated echo version (PFGSTE)^{31,32} of the pulsed field gradient spin echo technique (PFGSE), without slice selection. Thus, the propagator reported

here is volumetrically averaged over the total column cross section and over ca. 50 mm along the axial direction, i.e., over the homogeneous region covered by the solenoidal rf coil. Observation times Δ were varied in a range from 30 to 960 ms, and the repetition time between succeeding averages was fixed at 4 s, representing $5T_1$ of water in the porous packing. Each measurement was repeated for at least three times. Typically, $S(\mathbf{q}, \Delta)$ was acquired in the \mathbf{q} -space by making measurements for 64 values of $\mathbf{q} = \gamma\delta\mathbf{g}/(2\pi)$ in the range of $\pm\mathbf{q}_{\text{max}}$, with gradient amplitudes, \mathbf{g}_{max} , strong enough to attenuate the signal well down into the noise. The raw data then were processed using programs written in-house with IDL (Research Systems Inc., Boulder, CO). Prior to Fourier transformation they were zero-filled to 128 points, and the resulting propagator distributions were normalized for the different observation times chosen in the respective experiments.

Results and Discussion

Fluid particles located in different dynamic environments in the packed column can be quantitatively distinguished on the basis of their net migration distances (or dynamic displacements). For example, fluid molecules in the stagnant regions of the packed bed (like in the pore network inside the porous packing particles) do not contribute to the set of net displacements as long as their exchange with the flowing fraction is limited by the observation time chosen. An exchange between these two fractions takes place in the connected pore space (voids of the interparticle region of the packed bed and intraparticle pores). Thus, the actual dynamic displacement is determined by the average residence times spent in the stagnant and the flowing regions of the column, over the observation time Δ of the experiment (note that the stagnant fluid fraction includes both the internal pore volume of porous particles and the stagnant layer around all particles, porous or not. The latter being usually small compared to the former,³³ it will be neglected in this work). By measuring the dependence of the volume fractions of stagnant and flowing fluid particles on the observation time, the rate of mass transfer between these regions can be studied directly. Before discussing the experimental results, however, the origin and development of the classical convection-driven dispersion process in a packed bed of particles must be demonstrated. This will allow a clear visualization, differentiation, and quantitation of the stagnant mobile-phase fraction in a chromatographic column.

For short dynamic displacements (those which are of the order of a typical pore size of the packing particles), i.e., with $\bar{u}\Delta \ll d_p$, fluid transport in the interparticle void space can be viewed as occurring in randomly oriented capillaries (Figure 3a). Here, fluid molecules remain in individual capillaries over the whole observation time, Δ . At this length scale, they cannot experience any fork in the network of these external channels. They move at a constant velocity, given by the shape of the corresponding capillary and their position from the wall, and in a constant direction, given by the orientation of the channel. Thus, the averaged propagator recorded in this dynamic region yields directly the distribution of velocity components (in the direction of the field gradient), superimposed on the molecular diffusive displacements of the fluid molecules (which depends on the actual Peclet number of the experiment). In a bed made of porous particles, the displacements of the fluid molecules entrained in the internal pore network of the particles must also be considered. For short observation times, these molecules cannot participate in interparticle convective transport and are essentially restricted to diffusional transport inside the particle (cf. Figure 1).

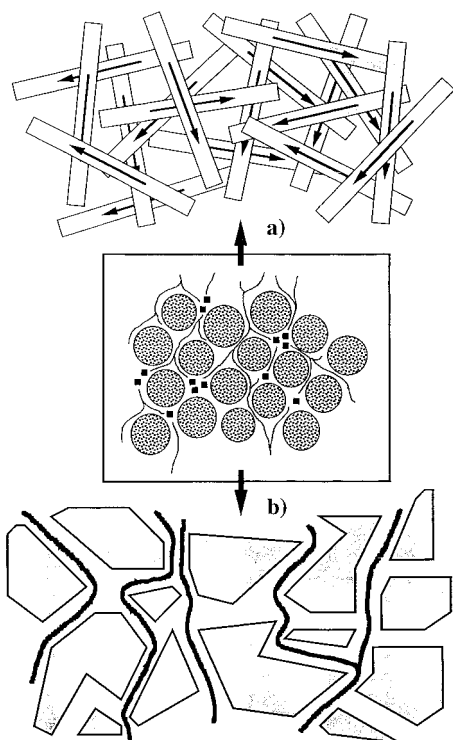


Figure 3. Convective transport in a packed bed of particles in different regimes. (a) $\bar{u}\Delta/d_p \ll 1$. The fluid molecules are moving in individual randomly oriented capillaries, with constant velocity and direction given by the shape/size and orientation of the capillary. (b) $\bar{u}\Delta/d_p \gg 1$. Now, flow occurs in branched capillaries, and the direction and magnitude of the velocity fluctuates according to the macroscopic flow rate chosen with respect to the dimension of the void space in the porous packing.

At the other extreme of the size of dynamic displacements, i.e., for $\bar{u}\Delta \gg d_p$, all fluid molecules experience the tortuous pore space (see Figure 3b). They reach various branches and move through several differently shaped and oriented capillaries. In this case, the (Gaussian) averaged propagator obtained corresponds to the classical dispersion process in a packed bed. For porous particles, this process includes also the exchange of fluid molecules between the interparticle void space and the intraparticle pore network. The observation time, Δ , is the critical parameter determining the relative importance of the two contributions to this process.

The onset of the velocity dependence of the dispersion process is demonstrated in Figure 4. Pure water is flushed through a 16 mm i.d. glass column packed with spherical-shaped porous silica particles of 50 μm average diameter. The observation time in this study is fixed ($\Delta = 30$ ms). Curve a in Figure 4 shows the averaged propagator acquired in the absence of flow. It is a Gaussian curve centered at a zero net displacement. Curves b–g correspond to stepwise increases of the flow rate. The averaged propagator becomes unsymmetrical because of the onset of net flow (b–d), and a shoulder develops at high flow rates (e–g). The formation of this shoulder is an intermediate step toward the Gaussian displacement probability distribution, which describes the classical axial dispersion process of fluid molecules percolating through a packed bed of particles (e.g., profile b in Figure 2). However, as shown by the broad rounded tops of the propagator distributions and the still important amount of net negative displacements (i.e., of those in the direction opposite to that of the flow), molecular diffusion is still a major component in the transport of fluid molecules (H_2O) at the highest flow rate and it cannot be neglected compared to convective displacements. For example,

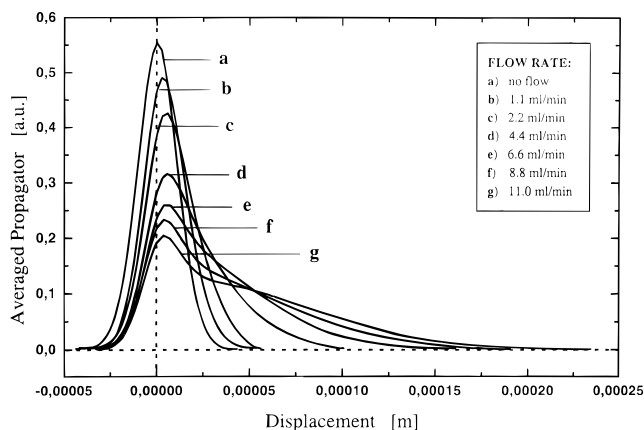


Figure 4. Axial averaged propagator distributions for water percolating through a 16 mm i.d. glass column packed with totally porous, spherical-shaped silica particles ($d_p = 50 \mu\text{m}$). Observation time Δ fixed at 30 ms, $\delta = 5.0$ ms. Volume flow rate, F_V , as indicated. Mobile phase: pure water.

under the experimental conditions for curve d, the root-mean-square (rms) translational displacement based on molecular diffusion alone is $(2D_m\Delta)^{1/2} \approx 11 \mu\text{m}$ (with $D_m = 2.15 \times 10^{-5} \text{ cm}^2/\text{s}$ at 23 $^\circ\text{C}$) while the convective (or net) displacement, based on $\bar{u}\Delta$, is around $15 \mu\text{m}$. At the highest flow rate, $F_V = 11 \text{ mL/min}$ corresponding to curve g, the convective displacement is $\bar{u}\Delta = 37.5 \mu\text{m}$. These figures show clearly that the contribution of molecular diffusion to the interstitial velocity distribution of the fluid molecules in a packed bed depends strongly on the molecular diffusivity of the probe compound and on the average particle size of the packing (D_m/d_p). In the present study this phenomenon is further complicated by the contribution of diffusion in the stagnant liquid-phase fraction, inside the porous particles. Thus, in order selectively to obtain velocity distributions in packed beds, it would be preferable to work with large diameter, nonporous particles, at values of the Peclet numbers high enough for the contribution of molecular diffusion to be negligible but low enough for the condition $\bar{u}\Delta \ll d_p$ to be valid.²⁰

For migration path lengths, $\bar{u}\Delta$, larger by respect to the particle diameter than those corresponding to the curves in Figure 4, the profile shoulder (best seen for curve g in Figure 4, at a convective displacement of ca. $5 \times 10^{-5} \text{ m}$) corresponding to convective displacements separates from the peak corresponding to diffusion in the stagnant liquid phase and develops into a complete Gaussian curve. Because larger dynamic displacements can be realized by increasing either the flow rate or Δ , we discuss now the effect of the observation time.

The effect of increasing Δ from 30 to 960 ms is illustrated in Figure 5. Curve a in this figure corresponds to the same experimental conditions as curve f in Figure 4 ($\Delta = 30$ ms, flow rate $F_V = 8.8 \text{ mL/min}$). The flow rate for all the other curves remains the same. The pure dispersive contribution around the zero displacement vanishes progressively when Δ is increased (curves b–e), and a single Gaussian shaped propagator is reached for $\Delta = 960$ ms, as shown by the enlarged curve f in Figure 5. No stagnant fluid fraction or random flow component (cf. Figure 3a) is left then, the exchange of fluid molecules between the deep pools of stagnant solvent in the porous particles and the stream flowing through the interparticle regions being complete. The apparent axial dispersion coefficient can be derived from a fit of the propagator distribution in curve f to a Gaussian profile or, alternately, from the standard deviation σ of the profile, calculated from its full width at half-

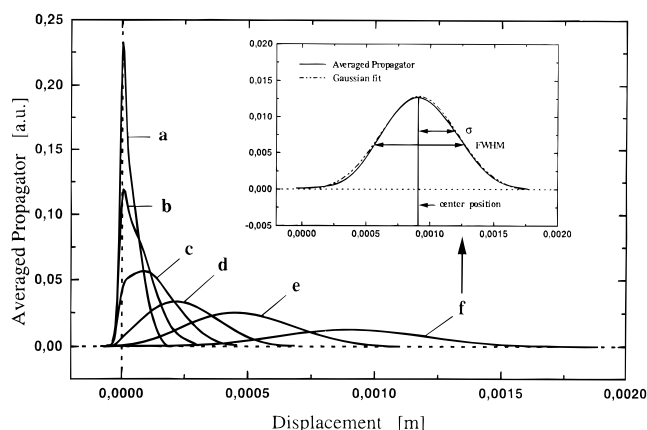


Figure 5. Axial displacement probability distributions, $F_V = 8.8$ mL/min. Observation times Δ : 30 ms (a), 60 ms (b), 120 ms (c), 240 ms (d), 480 ms (e), 960 ms (f). Glass column (16 \times 300 mm) packed with totally porous, 50 μ m (native) silica particles.

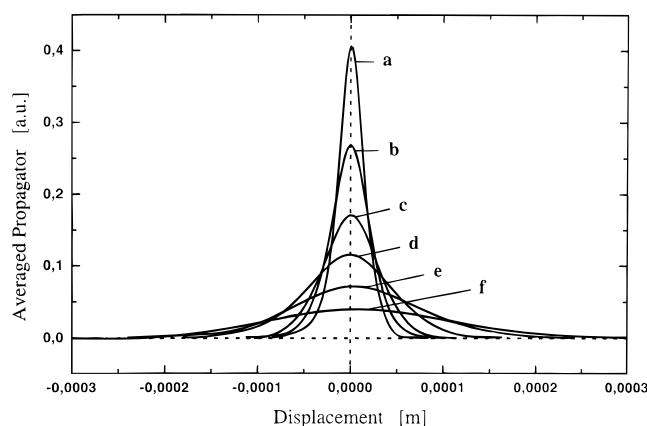


Figure 6. Transverse averaged propagator distributions, $F_V = 8.8$ mL/min. Observation times Δ : 30 ms (a), 60 ms (b), 120 ms (c), 240 ms (d), 480 ms (e), 960 ms (f). 16 mm i.d. glass column packed with porous silica particles ($d_p = 50$ μ m).

maximum, $\text{fwhm} = 2\sigma(2 \ln 2)^{1/2}$ with $\sigma^2 = 2D_{\text{ap}}\Delta$. We found $D_{\text{ap},a} = 4.7 \times 10^{-4}$ cm²/s. Furthermore, the dynamic displacement $\bar{u}\Delta$ determines the position of the center of the Gaussian distribution. Its measurement gives a direct estimate of the total column porosity, ϵ_T , since $\bar{u} = 4F_V/(\epsilon_T\pi d_c^2)$. From the center position at 958 μ m (curve f) a value $\epsilon_T = 0.73$ is derived. The center positions $\bar{u}\Delta$ of the distributions d, e, and f are exactly proportional to the values of Δ , the values of $\bar{u}\Delta$ and Δ being 239.5 μ m and 240 ms (curve d), 479.3 μ m and 480 ms (curve e), 958.3 μ m and 960 ms (curve f), respectively.

Figure 6 shows the results of the same measurements as those reported in Figure 5 but now performed in the transverse direction of the column, i.e., perpendicular to the net flow direction. In this case, all the displacement probability distributions are centered at a zero net displacement, an expected result since there is no net flow in the transverse direction. Compared to the corresponding axial displacement distributions, measured at the same observation time Δ and shown in Figure 5, the transverse propagator distributions (Figure 6) are much narrower because the transverse dispersion coefficient is much lower than the axial one at the flow rate chosen for both sets of measurements ($F_V = 8.8$ mL/min). For example, at $\Delta = 960$ ms, the value of $D_{\text{ap},t} = 4.2 \times 10^{-5}$ cm²/s (curve f, Figure 6) is more than 10 times less than that of $D_{\text{ap},a} = 4.7 \times 10^{-4}$ cm²/s (see above, curve f, Figure 5).

We have discussed so far results obtained under such experimental conditions that the distribution of displacements

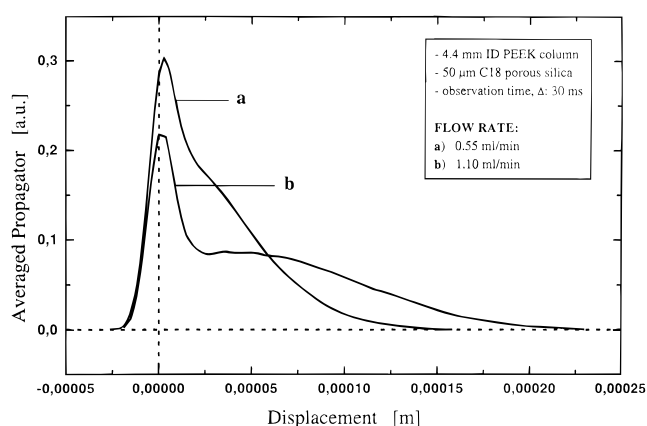


Figure 7. Axial averaged propagator distributions. Flow rate, F_V : 0.55 mL/min (a), 1.1 mL/min (b). Observation time $\Delta = 30$ ms. 4.4 mm i.d. PEEK column packed with totally porous, spherical-shaped C18 silica particles ($d_p = 50$ μ m). Mobile phase: pure water.

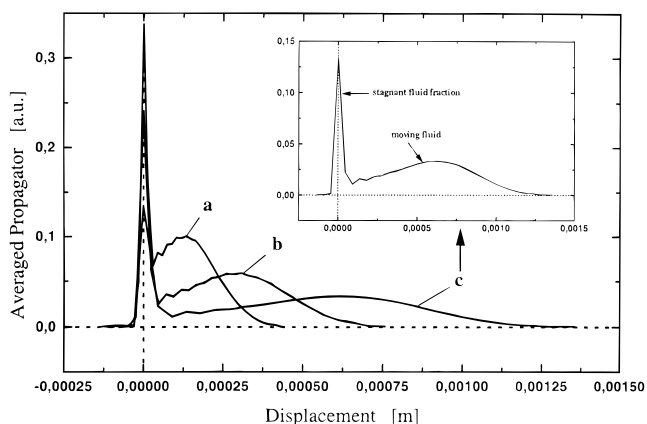


Figure 8. Displacement probability distributions obtained from measurements performed in the direction of flow (Figure 7 continued), with flow rates, F_V : 2.2 mL/min (a), 4.4 mL/min (b), and 8.8 mL/min (c).

has either a large mode at zero for dispersive displacements and a hump for finite convective displacements (curves b–g in Figure 4, curves a and b in Figure 5) or a large mode at a finite migration distance with no mode corresponding to the dispersive displacements (curves d–f in Figure 5). It would be interesting to carry out the same measurements under such experimental conditions that the dispersive displacement spike at zero displacement would be resolved from the convective displacement distribution before disappearing. This study was done by increasing the flow rate (hence, $\bar{u}\Delta$) at a fixed observation time. Because the pump available had a maximum flow rate of ca. 11 mL/min, larger displacements with respect to the support particle are achieved by using the narrower 4.4 mm i.d. PEEK column, packed with totally porous, chemically bonded C18 silica particles having a 50 μ m average diameter. Thus, the average particle diameter remains the same, while the column diameter is reduced from 16 to 4.4 mm. The results of this series of measurements at increasing flow rates (and a fixed observation time, $\Delta = 30$ ms) are reported in Figures 7 and 8.

The first displacement probability distribution shown in Figure 7 (curve a) corresponds approximately to the same dynamic situation as that for curve g in Figure 4, exhibiting a significant shoulder. The shoulder at high displacements is clearly visible. The distribution b in Figure 7 exhibits what looks as the second half of a Gaussian profile. This developing trend is completed in Figure 8, in which the separation of the two Gaussian distributions in the displacement space can be

followed directly as the ratio $\bar{u}\Delta/d_p$ is increased up to ca. 8.6 (curve c in Figure 8). This last profile is enlarged in the inset and shows a distinct bimodal feature. One mode is the broad Gaussian part of the averaged propagator, which characterizes convective dispersion of the water molecules in the packed bed. The second mode is a narrow Gaussian curve, centered exactly at zero net displacement. It seems to be independent of the flow rate chosen. It corresponds to stagnant molecules. These results show that the discrimination of the fluid molecules based on their net migration distances increases with increasing flow rates. Obviously, this bimodal behavior arises from the incomplete exchange of the water molecules that can take place between the stagnant pools inside the particles and the stream percolating across the column bed during the experimental observation time ($\Delta = 30$ ms).

It is possible to resolve these two dynamic modes, to calculate their volume fractions, and to derive the dispersion coefficients of the water molecules in the respective environments. This is achieved by taking the absolute of the echo attenuation raw data, $S(\mathbf{g}, \delta, \Delta)/S(0, \delta, \Delta)$, and fitting them to a biexponential expression (each one of them similar to the monoexponential one in eq 7) that simply represents a summation of the contributions of both fluid fractions to dispersion¹⁹

$$E(\mathbf{g}, \delta, \Delta) = \frac{S(\mathbf{g}, \delta, \Delta)}{S(0, \delta, \Delta)} = \sum_{i=1}^2 A_i \exp[-\gamma^2 \delta^2 \mathbf{g}^2 D_{ap,i} \{\Delta - \delta/3\}] \quad (10)$$

where A_i denotes the respective volume fractions and $\{\Delta - \delta/3\}$ is the effective (or reduced) observation time that accounts for the finite duration of the gradient pulses (δ) used in practice. The equation in the form presented above assumes that the relaxation times of the fluid molecules in both phases are invariant. In fact, a possible dependence of the respective volume fractions on the observation time due to different longitudinal relaxation times (T_1) could be associated with the PFG stimulated echo sequence used in our studies. In the general case, such an effect has to be considered, but it was found insignificant in the present case (with insignificant wall relaxation effects of the water molecules at the hydrophobic C-18 layer bonded to the internal surface of the silica particles). For the averaged propagator distribution shown as curve b in Figure 7, the raw data acquired in the \mathbf{q} -space and the best fit of these data to eq 10 are shown in parts a and b of Figure 9, respectively. The data acquired in the \mathbf{q} -space (Figure 9a) clearly show a characteristic bi-Gaussian distribution with the same center and different variances. Upon Fourier transformation a bi-Gaussian distribution is obtained, this time in the displacement space. This is the displacement probability distribution shown as curve b in Figure 7. The best biexponential fit applied to the raw data (Figure 9b) gives (with $r^2 = 0.998$): $D_{ap,1} = 8.1 \times 10^{-4}$ cm²/s, $A_1 = 79\%$, and $D_{ap,2} = 9.7 \times 10^{-6}$ cm²/s, $A_2 = 21\%$.

The former contribution originates from the fluid molecules that undergo convection-driven dispersion in the packing (with $\nu = \bar{u}d_p/D_m = 42$), while the latter results from the dispersion of the fluid molecules in regions of the column occupied by essentially stagnant liquid phase. In these stagnant pools, the apparent diffusivity is reduced by a factor of 2.21 compared to the molecular diffusivity of pure water ($D_{ap} = 9.7 \times 10^{-6}$ cm²/s as compared to $D_m = 2.15 \times 10^{-5}$ cm²/s). Both the center position of the mode at zero net displacement and the value of

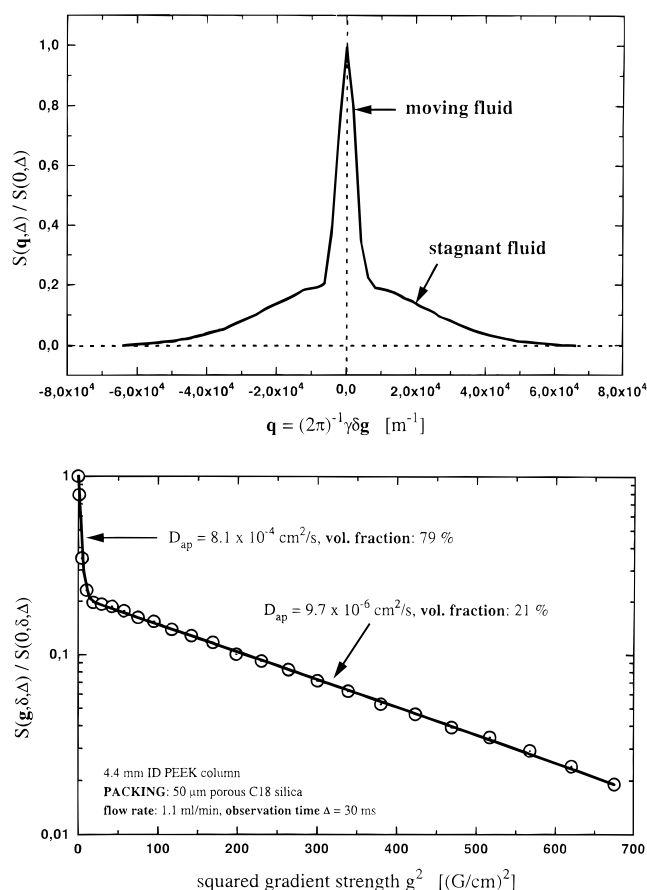


Figure 9. (a, top) Absolute of the normalized echo signal $S(\mathbf{q}, \Delta)/S(0, \Delta)$ as acquired in \mathbf{q} -space, with $\mathbf{q} = \gamma\delta\mathbf{g}/(2\pi)$. 64 equidistant \mathbf{q} -steps between $\pm\mathbf{q}_{\max}$, symmetrically distributed around $\mathbf{q} = 0$, with four phase-alternated averages taken at each \mathbf{q} -step. Observation time $\Delta = 30$ ms, $\delta = 4.5$ ms. 4.4 mm i.d. PEEK column packed with the 50 μm C18 silica particles, mobile phase: pure water. Flow rate, F_V : 1.1 mL/min. The \mathbf{q} -vector is oriented parallel to the flow direction. (b, bottom) $S(\mathbf{g}, \delta, \Delta)/S(0, \delta, \Delta)$ of Figure 9a vs the squared gradient amplitude, g^2 , and the best fit (solid line) to the experimental data (open circles) using eq 10.

the apparent dispersion coefficient identify the corresponding water molecules, accounting for ca. 21% of the water in the column, as molecules that are severely hindered from exchange with the regions of net flow. Inside the totally porous support particles, which have an average pore diameter of 120 Å, the effective diffusion coefficient is significantly reduced as compared to the molecular diffusivity (see later).

The theory presented earlier was used to calculate the velocity dependence of the stagnant and flowing fluid fractions under the experimental conditions reported in Figures 7 and 8. All the averaged propagator distributions measured showed a clear bimodal (Gaussian) displacement distribution pattern, as illustrated in Figure 9a,b. The results obtained are shown in Figure 10. Beyond ca. 1 mL/min, the two volume fractions are independent of the flow rate. This suggests that a diffusion-limited exchange process—independent of the column cross-sectional average velocity—is responsible for this behavior. Because the observation time, Δ , remains constant at 30 ms in this whole series of measurements, the extent of diffusional mass transfer is limited to what can take place during this time. The stagnant fluid fraction being defined on the basis of the relative area of the contribution with a zero net displacement, an amount of 21% of the water in the column remains unexchanged.

Obviously, the next step is to determine the variation of the relative fluid volume fractions with Δ by investigating the effect

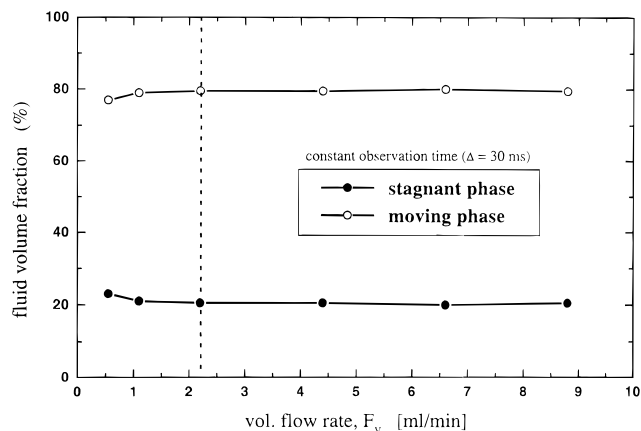


Figure 10. Stagnant and net displaced fluid (water) fractions in the packed bed as a function of the flow rate, F_V . Observation time $\Delta = 30$ ms. Calculations are based on eq 10, using the raw data of the results shown in Figures 7 and 8. 4.4×150 mm PEEK column packed with the porous $50 \mu\text{m}$ C18 silica particles.

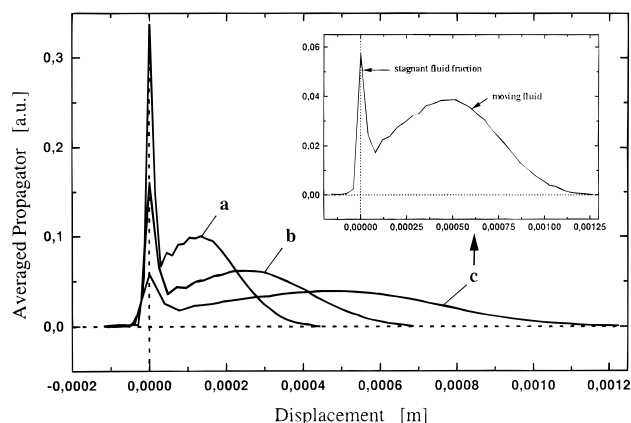


Figure 11. Axial averaged propagator distributions in dependence of the observation time Δ . Flow rate, $F_V = 2.2$ mL/min. Observation times Δ : 30 ms (a), 60 ms (b), 120 ms (c); $\delta = 4.0$ ms. 4.4 mm i.d. PEEK column packed with porous C18 silica particles ($d_p = 50 \mu\text{m}$). Mobile phase: pure water.

on a bimodal displacement probability distribution of an increase of the observation time at constant flow rate. Measurements were made under the experimental conditions used to acquire the averaged propagator distribution shown as curve a in Figure 8 ($\Delta = 30$ ms, $F_V = 2.2$ mL/min). Under these conditions, the two volume fractions were found to be independent of the flow rate (see the dotted line in Figure 10).

Typical results are reported in Figures 11 and 12. They are similar to those reported earlier, in Figures 7 and 8. For example, curve a in Figure 11 corresponds to curve a in Figure 8. The observation time is doubled from one curve to the next, beginning with 30 ms for curve a in Figure 11 and ending with 960 ms for curve c in Figure 12. While the molecules in the stream of fluid percolating through the bed migrate over longer and longer distances with increasing Δ (according to the dynamic parameter $\bar{u}\Delta$), the fraction of stagnant fluid prevented from exchanging with the fluid stream decreases continuously. It has entirely disappeared at $\Delta = 960$ ms (curve c in Figure 12). For example, at $\Delta = 120$ ms (curve c in Figure 11, enlarged in the inset), the relative volume of the stagnant fluid fraction has decreased to 8.5% (from the original 20% at $\Delta = 30$ ms). At $\Delta = 960$ ms (curve c in Figure 12, enlarged in the inset), the averaged propagator distribution has become a single Gaussian. In all cases, the total porosity of the bed can be derived from the center position of the convective displacement

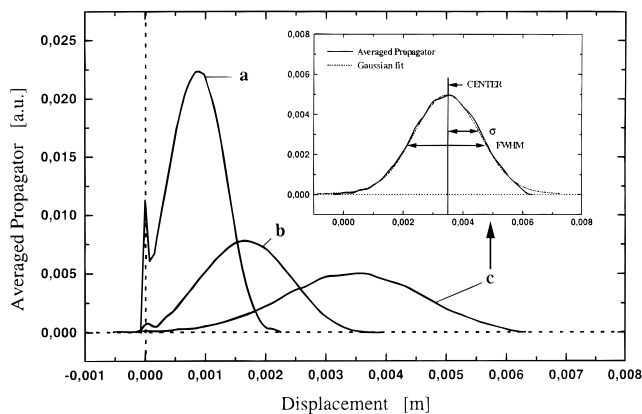


Figure 12. Axial displacement probability distributions (continued from Figure 11), with observation times Δ : 240 ms (a), 480 ms (b), and 960 ms (c); $\delta = 3.5$ ms.

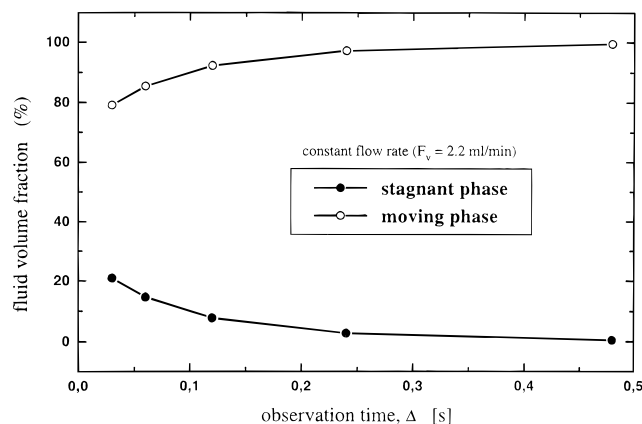


Figure 13. Stagnant and net displaced water volume fractions in the packed bed in dependence of the observation time Δ . Flow rate, $F_V = 2.2$ mL/min. Calculations are based on eq 10, using the raw data of the displacement probability distributions shown in Figures 11 and 12.

mode (eq 9). For $\Delta = 960$ ms, the dynamic displacement is $3458 \mu\text{m}$ and $\epsilon_T = 0.67$, in reasonable agreement with the value of 0.73 derived from the data in Figure 5 ($\Delta = 30$ ms). A necessary prerequisite for this determination is that the fluid molecules probe the total connected pore space, i.e., that the exchange between the fluid phase in the internal and external pore volumes be complete and a single Gaussian displacement probability distribution be observed (as e.g., curve c in Figure 12). For example, for the bimodal distribution obtained at $\Delta = 30$ ms (curve a in Figure 11), the position of the center of the Gaussian profile corresponding to the convective displacements is located at a (net) displacement of $131 \mu\text{m}$. Accordingly, the fluid particles constituting this Gaussian "feel" a total porosity of only 0.55 because the exchange of molecules of the liquid stream with the stagnant fluid molecules (the latter causing the Gaussian centered at a zero net displacement) is incomplete. In the limit of $\Delta \rightarrow 0$, the exchange is completely hindered and the position of the net displaced Gaussian should correspond to the interparticle porosity of the packed bed, typically around 0.38–0.40 for analytical columns.

The volume fractions of stagnant and flowing liquid phase derived from the experiments reported above are plotted vs the observation time in Figure 13. The volume fraction of the stagnant fluid is plotted separately in Figure 14 vs the observation time. The latter is normalized by the exchange time (see later, eq 11) in order to allow direct comparison with the data discussed later for a material made of $15 \mu\text{m}$ particles. At Δ

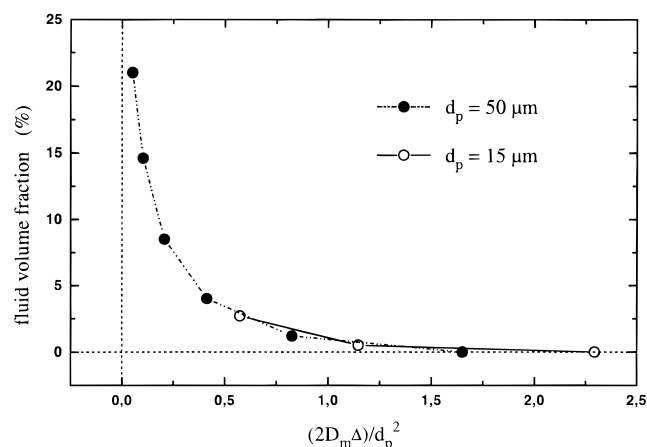


Figure 14. Stagnant mobile-phase fraction (taken from either Figure 13 or similar data for the 15 μm particles column that is discussed later) plotted separately vs the normalized time, $2D_m\Delta/d_p^2$ (Δ from 30 to 480 ms for the 50 μm particles and from 30 to 120 ms for the 15 μm particles). Flow rate, $F_V = 2.2$ mL/min. Mobile phase: pure water.

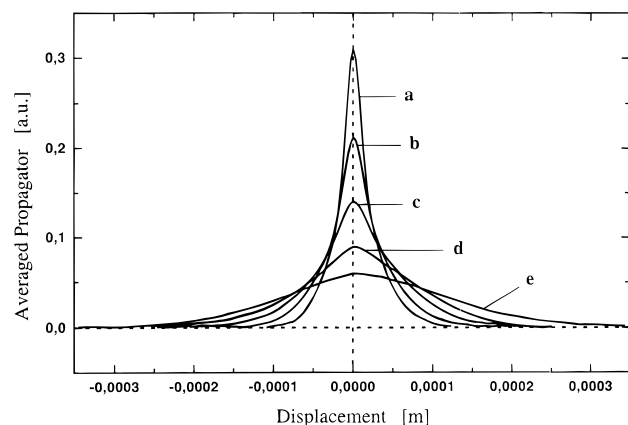


Figure 15. Transverse averaged propagator distributions as a function of the observation time Δ . Flow rate, $F_V = 2.2$ mL/min. Observation times Δ : 30 ms (a), 60 ms (b), 120 ms (c), 240 ms (d), 480 ms (e); $\delta = 4.0$ ms. 4.4×150 mm PEEK column packed with porous 50 μm C18 silica particles. Mobile phase: pure water.

= 480 ms (curve b in Figure 12), this fraction is only 0.5–1% of the total fluid molecules in the column.

Figure 15 shows the transverse averaged propagator distributions derived under the same set of experimental conditions as the axial distributions shown in Figures 11 and 12 (i.e., $F_V = 2.2$ mL/min, variable Δ , from 30 to 480 ms). These distributions are similar to the one shown in Figure 9 and lead to the same conclusions as derived from the study of the axial displacement probability distributions. They exhibit a distinct bimodal Gaussian behavior at short observation times. The profiles of the distributions tend toward a single Gaussian with increasing observation times (see curves a–e in Figure 15). The two Gaussian components correspond to the dispersions of the fluid molecules undergoing transverse dispersion inside the porous packing and of those migrating with the fluid percolating through the bed of particles, respectively. The bimodal character of the distributions is not as clear for the transverse displacement probability distribution as for the axial one because (as noted earlier, see Figure 6) both Gaussian contributions are centered at the zero net displacement. They still can be distinguished, however, on the basis of their different dispersion characteristic (i.e., by fitting the experimental data to eq 10).

In summary, the experimental data presented so far give quantitative estimates of the mass-transfer resistances that take

place in a packed chromatographic column between the stagnant, intraparticle liquid phase and the stream of liquid phase percolating through the bed. They allow the quantitative study of the exchange process between these two phases. These data provide strong evidence for a diffusion-limited mass-transfer kinetics between the interstitial void space of the packed bed and the deep pools of stagnant mobile phase held in the small pores of the 50 μm particles used (see, for example, Figures 10 and 13). These results are now compared to independent results obtained by other approaches more conventionally used in chromatography.

The transport behavior data obtained must be related to the average particle size ($d_p = 50$ μm), to the average diameter of the channels between close particles in a packed bed and to the average pore size. The average pore diameter of the totally porous C18 bonded silica particles used in this work is approximately 130 \AA (130 ± 15 \AA as given by the manufacturer³⁴). The average diameter of the channels available to the stream of liquid phase are of the order of 5–8 μm (10–15% of d_p ³⁵). Owing to the fact that the mean flow velocity through a network of interconnected pores depends on the square of the average pore diameter, the average velocity of the fluid molecules in the small pores of the particles is approximately 2×10^{-5} smaller than that in the interparticle space (assuming that the pores are well-interconnected)⁵. The intraparticle pore architecture and its anastomosis are more complex than those of the interparticle void space, resulting in a more hindered diffusion process, i.e., a higher tortuosity. The stagnant pools encountered inside the 50 μm particles used in our work are deeper than usual in analytical chromatography and best suited for a study of the slow diffusional steps occurring during mass transfer therein. The average diffusion lengths for water molecules are $l_D = (2\Delta D_m)^{1/2} = 11$ and 63 μm at observation times of 30 and 960 ms, respectively. This illustrates the importance of diffusional resistances to mass transfer at short observation times (compare, for example, curve a in Figure 11 and curve c in Figure 12).

In order to achieve complete exchange between the stagnant and the moving fluid, diffusion within a porous particle must carry a molecule from the particle center to the particle boundary, over a straight distance of $d_p/2$ (25 μm). Reformulating Einstein law of diffusion for this particular case,⁵ we obtain for the exchange time, t_e , required to achieve complete exchange by diffusion

$$t_e = \frac{1}{2D_m} \left(\frac{d_p}{2} \right)^2 \quad (11)$$

With the molecular diffusivity of pure water, an exchange time of $t_e = 145$ ms is derived from eq 11. This is in agreement with the result given earlier that, at an observation time of $\Delta = 120$ ms, the stagnant volume fraction of water is still 8.5% (curve c in Figure 11). Furthermore, molecular diffusion across the particles cannot take place in a straight direction from the center to the boundary. The rate of mass transfer depends on the intraparticle tortuosity and, in turn, on the interconnectivity of the small intraparticle pores. The intraparticle tortuosity, γ_{intra} , is the ratio of the apparent or effective diffusivity of the fluid phase inside the particles, D_∞ , and the molecular diffusivity D_m .^{36,37} (Note that, unfortunately, the tortuosity coefficient is defined in chromatography as the reverse of the coefficient defined in the materials sciences and in chemical engineering.)

Each experiment reported earlier (cf. Figures 5, 7, and 8) allows the calculation of a value of the diffusion coefficient of

the water molecules in the stagnant mobile phase. The values obtained are all between 9.5×10^{-6} and 1.15×10^{-5} cm²/s, to be compared to $D_m = 2.15 \times 10^{-5}$ cm²/s at 23 °C. This result suggests values for the chromatographic intraparticle tortuosity of the particles studied between 0.44 and 0.53 ($\gamma_{\text{intra}} = D_{\text{ool}}/D_m$), corresponding to a range of conventional tortuosities T ($\gamma_{\text{intra}} = 1/T$) between 1.87 and 2.27.

For columns randomly packed with nonporous spheres and having an interstitial porosity close to 0.40, the tortuosity factor, γ_{inter} , for unretained fluids was found to be approximately 0.65.^{38–40} The value found for γ_{intra} shows that diffusion within the stagnant mobile phase impregnating the porous particles is more hindered than it is in a packing of random spheres. Because the degree of obstruction and constriction is higher in the intraparticle pore network than in the extraparticle one and the pore connectivity lower, the internal tortuosity, γ_{intra} , is somewhat lower than 0.6, a value previously assumed.⁴¹ The exact value is obviously an important property of a packing material.

Recently, Gibbs et al.³⁷ have used ¹H and ¹⁹F PFGNMR to study protein diffusion (i.e., tracer diffusion) in the porous particles of materials used for gel filtration chromatography (average particle diameters, $d_p = 30$ and $45 \mu\text{m}$). They described a method for the selective measurement of intraparticle diffusional behavior, eliminating the contribution of interparticle transport. A tortuosity factor of $T = 2.2 \pm 0.4$ was found for the entire protein concentration range studied. This value is close to the one derived for an isotropic porous medium made of sinuous capillaries or pores, i.e., 2,⁴² while typical tortuosity factors found for real porous solids range between 1.5 and 6.⁴³ On the other hand, a tortuosity factor of 3 was predicted for isotropic pore systems made of straight, nonintersecting, cylindrical pores, with no dead-end branches.⁴⁴ On the basis of the examination of microphotographs, Gibbs et al.³⁷ concluded that the typical “popcorn ball” geometry of the porous particles used in their studies accounts well for the value that they obtained for the tortuosity factor, around 2.2 and close to the isotropic porous medium value of 2.⁴² The values of the tortuosity factors obtained in our experiments ($T = 1.9–2.3$), the spherical shape of the porous silica particles, and what is known of their pore structure¹⁴ combine strongly to favor the isotropic porous medium model, also. However, it should be noted that we did not use a sorbed tracer, but instead took the mobile phase (water) itself as a probe of the inter- and the intraparticle fluid dynamic displacements within one and the same measurement. In our experiments, the fluid molecules carried inside the particles (over time Δ) could be identified and measured quantitatively on the basis of their zero net migration displacement in the presence of externally driven convection.

If the average diameter of the porous particles is changed without changing their shape or the intraparticle morphology, that is hopefully the case when particles of the same brand are used, the mass-transfer resistances in the stagnant mobile phase should scale with d_p^2 according to eq 11. For this purpose, we used $15 \mu\text{m}$ spherical-shaped, totally porous C18 silica particles of the same YMC brand as the $50 \mu\text{m}$ particles used in the experiments reported earlier. They had the same average pore size of 130 \AA .³⁴ They were packed in a $4.4 \times 150 \text{ mm}$ PEEK column. Now, the exchange time calculated from eq 11 is $t_e = 13 \text{ ms}$. The results obtained under the same conditions are shown in Figures 16–18. Figure 16 shows the axial displacement probability distributions obtained at different flow rates, with a constant observation time ($\Delta = 30 \text{ ms}$). In this case,

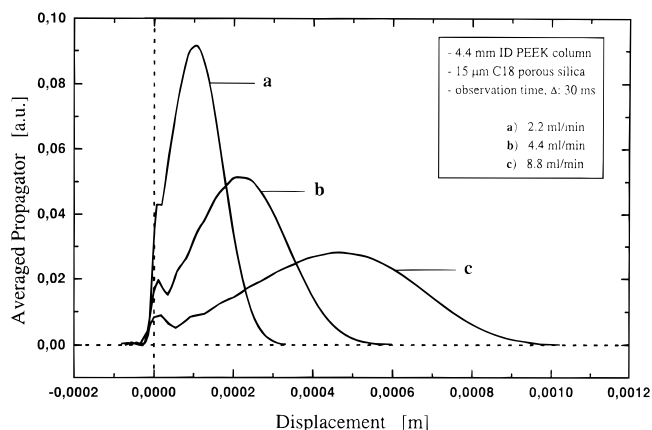


Figure 16. Axial displacement probability distributions in dependence of the flow rate, F_V : 2.2 mL/min (a), 4.4 mL/min (b), and 8.8 mL/min (c). Observation time $\Delta = 30 \text{ ms}$. $4.4 \times 150 \text{ mm}$ PEEK column packed with totally porous, spherical-shaped C18 silica particles ($d_p = 15 \mu\text{m}$).

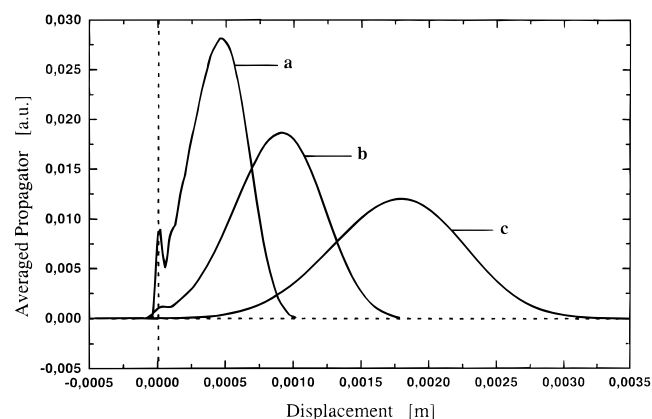


Figure 17. Axial averaged propagator distributions, $F_V = 8.8 \text{ mL/min}$. Observation times Δ : 30 ms (a), 60 ms (b), 120 ms (c); $\delta = 3.5 \text{ ms}$. Mobile phase: pure water.

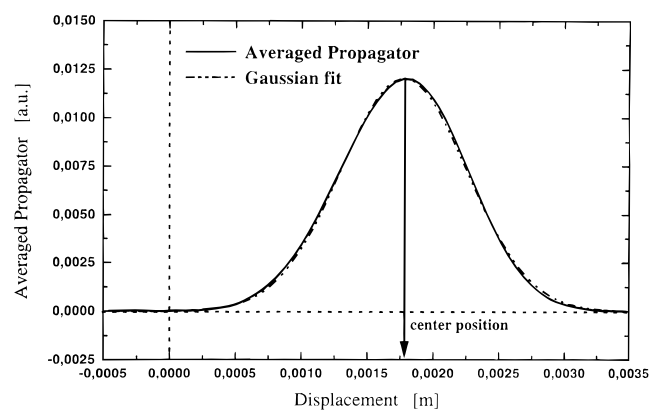


Figure 18. Axial averaged propagator distribution (i.e., (c) of Figure 17) and best single Gaussian fit applied to the displacement data. Flow rate, $F_V = 8.8 \text{ mL/min}$, observation time $\Delta = 120 \text{ ms}$. 4.4 mm i.d. PEEK column packed with the porous C18 silica particles of $15 \mu\text{m}$ average diameter. $D_{\text{ap,a}} = \sigma^2/2\Delta = 9.52 \times 10^{-3} \text{ cm}^2/\text{s}$; $\epsilon_T = 0.65$.

only 2.5 % of the water molecules are left unexchanged in the stagnant volume fraction of the liquid phase, at zero net displacement (versus 21% with the $50 \mu\text{m}$ particles). As in the case of these larger particles (cf. Figure 8), this fraction is independent of the flow rate.

Figure 17 shows the axial displacement probability distributions obtained at different observation times (Δ) with a constant flow rate ($F_V = 8.8 \text{ mL/min}$). Note that the distributions c in Figure 16 and a in Figure 17 are identical. At a Δ of 60 ms

(curve b in Figure 17), the dispersive displacements in the stagnant fluid contribute only by a small shoulder to the distribution. For $\Delta = 120$ ms (curve c in Figure 17) the distribution includes a single Gaussian profile. All the water molecules are then exchanged between the two fractions of the liquid phase during the observation time. This last displacement probability distribution is compared in Figure 18 to its best fit to a Gaussian profile. From the center position at $\bar{u}\Delta = 1775$ μm of this curve, a value $\epsilon_T = 0.65$ is calculated for the total porosity. It is slightly lower than that obtained for the 4.4×150 mm PEEK column packed with the 50 μm particles (0.67). This small difference is in agreement with the column-to-column reproducibility achieved in the packing of chromatographic columns.⁴⁵

Using eq 10 again to resolve the contributions of the two volume fractions of the liquid phase to the bimodal distributions shown in Figure 16, we obtain for the stagnant fluid fraction a dispersion coefficient around 1.1×10^{-5} cm^2/s . For example, the best biexponential fit to the raw data of the displacement distribution a in Figure 16 gives (with $r^2 = 0.9993$): $D_{\text{ap},1} = 7.55 \times 10^{-4}$ cm^2/s , $A_1 = 97.3\%$, and $D_{\text{ap},2} = 1.05 \times 10^{-5}$ cm^2/s , and $A_2 = 2.7\%$. The value obtained for $D_{\text{ap},2}$ is close to the one calculated for the effective diffusion coefficient in the stagnant mobile phase inside the 50 μm C18 silica particles. This suggests that the internal pore networks of the particles of the two packing materials are very similar and that the main difference between the two packed columns is in the different size of the particles used ($d_p = 15$ and 50 μm). This result is confirmed by the data in Figure 14, which compares the plots of the fluid fraction of the liquid phase unexchanged by diffusion versus the root mean square of the diffusive displacement (i.e., $(2D_m\Delta)^{1/2}$), normalized by the average particle diameter for the two materials used. The two sets of data overlay exactly.

Conclusions

The methodology and the results presented in this report clearly demonstrate the major contribution that the PFGNMR techniques may bring to fundamental, technological, and comparative studies of the fluid dynamics in porous media. These techniques allow the quantitative determination of the relative amounts of stagnant (i.e., purely diffusive) fluid pools in a packed bed of porous particles and of the fluid stream in which molecules are in a convective environment. They allow also a detailed investigation of the kinetics of the mass transfer between these two different fluid fractions. The observation time that is used as an adjustable parameter in these experiments can be accurately set and easily adjusted. The derivation of accurate estimates of the average velocity of the mobile phase, of the total porosity of the packing, and of the volume fraction of the unexchanged fraction of the stagnant mobile phase at different mobile phase velocities are easily carried out from the averaged propagator which is supplied by simple manipulation of the motion-encoded signals obtained in PFGNMR. Thus, by operating the chromatographic columns under steady flow, a dynamic situation which is typical for chromatography is generated, and data relevant to the kinetics of mass transfer in chromatography can be collected.

This noninvasive method will allow the differentiation between various packing materials used as stationary phases in chromatography, the correlation between chromatographic properties controlled by the mass-transfer kinetics, e.g., column efficiency, and the internal tortuosity of their particles. They provide an original, accurate, and independent method of determination of the mass-transfer resistances, especially at high

Peclet numbers (i.e., mobile-phase velocities). The dependence of these properties on the internal and external porosities, on the average pore size, and on the parameters of the pore size distributions becomes possible, as well as the study of the pore connectivity and the investigation of a possible, albeit yet elusive, perfusion effect. When combined with NMR imaging methods, the PFGNMR techniques would allow the determination and the visualization of the dynamic properties of fluids in packed columns, and more generally in beds packed with particles having a low concentration in paramagnetic impurities on a microscopic scale. It would be possible to determine local fluctuations of the column external porosity, of its external tortuosity, of the mobile-phase velocity, of the axial and transverse dispersion coefficients, and of the parameters of the mass-transfer kinetics discussed in the present work. Thus, dynamic NMR microscopy²⁹ has the potential to determine the dynamic anatomy of chromatographic columns and to allow the unravelling of many secrets still vexing chromatographers.⁴⁶

Acknowledgment. This work was supported by a Human Capital and Mobility Grant ERBCHGECT-940061 of the European Union. Dr. Ulrich Trüdinger (YMC Europe, Schermbach, Germany) kindly provided the packing materials used in this study. We also thank Frank Vergeldt for computational assistance. This work was also supported in part by Grant DE-FG05-88ER13859 of the U.S. Department of Energy and by the cooperative agreement between the University of Tennessee and the Oak Ridge National Laboratory.

References and Notes

- (1) Martin, A. J. P.; Synge, R. L. M. *Biochem. J.* **1941**, *35*, 1358.
- (2) Boyd, G. E.; Adamson, A. W.; Meyers, L. S., Jr. *J. Am. Chem. Soc.* **1947**, *69*, 2836.
- (3) Boyd, G. E.; Meyers, L. S., Jr.; Adamson, A. W. *J. Am. Chem. Soc.* **1947**, *69*, 2849.
- (4) Kasten, P. R.; Lapidus, L.; Amundson, N. R. *J. Phys. Chem.* **1952**, *56*, 683.
- (5) Giddings, J. C. *Dynamics of Chromatography*; Marcel Dekker: New York, 1965.
- (6) Glueckauf, E. *Trans. Faraday Soc.* **1955**, *51*, 1540.
- (7) Snyder, L. R. *J. Chromatogr. Sci.* **1969**, *7*, 352.
- (8) Klinkenberg, A.; Sjenitzer, F. *Chem. Eng. Sci.* **1956**, *5*, 258.
- (9) van Deemter, J. J.; Zuiderweg, F. J.; Klinkenberg, A. *Chem. Eng. Sci.* **1956**, *5*, 271.
- (10) Done, J. N.; Knox, J. H. *J. Chromatogr. Sci.* **1972**, *10*, 606.
- (11) Huber, J. F. K. *J. Chromatogr. Sci.* **1969**, *7*, 85.
- (12) Unger, K. K.; Jilge, G.; Kinkel, J. N.; Hearn, M. T. W. *J. Chromatogr.* **1986**, *359*, 61.
- (13) Horváth, Cs.; Lipsky, S. L. *Anal. Chem.*, **1967**, *39*, 11.
- (14) Unger, K. K. *Silica and Chromatography*; Elsevier: Amsterdam, The Netherlands, 1979.
- (15) Liapis, A. I. *Math. Modell. Sci. Comput.* **1994**, *1*, 397.
- (16) van Kreveld, M. E.; van den Houd, N. *J. Chromatogr.* **1978**, *149*, 71.
- (17) Frey, D. D.; Schweinheim, E.; Horváth, Cs. *Biotechnol. Prog.* **1993**, *9*, 273.
- (18) Liapis, A. I.; McCoy, M. A. *J. Chromatogr.* **1992**, *599*, 87.
- (19) Callaghan, P. T. *Principles of Nuclear Magnetic Resonance Microscopy*; Clarendon Press: Oxford, 1993.
- (20) Lebon, L.; Oger, L.; Leblond, J.; Hulin, J. P.; Marty, N. S.; Schwartz, L. M. *Phys. Fluids* **1996**, *8*, 293.
- (21) Waggoner, R. A.; Fukushima, E. *Magn. Reson. Imaging* **1996**, *14*, 1085.
- (22) Packer, K. J.; Tessier, J. J. *Mol. Phys.* **1996**, *87*, 267.
- (23) Tessier, J. J.; Packer, K. J.; Thovet, J.-F.; Adler, P. M. *AIChE J.* **1997**, *43*, 1653.
- (24) Kärger, J.; Heink, W. *J. Magn. Reson.* **1983**, *51*, 1.
- (25) Cory, D. G.; Garroway, A. N. *Magn. Reson. Med.* **1990**, *14*, 435.
- (26) Stejskal, E. O. *J. Chem. Phys.* **1965**, *43*, 3597.
- (27) Stejskal, E. O.; Tanner, J. E. *J. Chem. Phys.* **1965**, *42*, 288.
- (28) Callaghan, P. T.; Coy, A.; MacGowan, D.; Packer, K. J.; Zelaya, F. O. *Nature* **1991**, *351*, 467.
- (29) Callaghan, P. T.; Xia, Y. *J. Magn. Reson.* **1991**, *91*, 326.

- (30) Poole, C. F.; Poole, S. K. *Chromatography Today*, 2nd ed.; Elsevier: Amsterdam, 1993; Section 4.3.
- (31) Tanner, J. E. *J. Chem. Phys.* **1970**, *52*, 2523.
- (32) Kärger, J.; Pfeifer, H.; Heink, W. *Adv. Magn. Reson.* **1988**, *12*, 1.
- (33) Tallarek, U.; Bayer, E.; Guiochon, G. *J. Am. Chem. Soc.* **1998**, *120*, 1494.
- (34) *Liquid Chromatography Product Guide*; YMC Inc.: Wilmington, NC.
- (35) Guan, H.; Guiochon, G.; Davis, E.; Gulakowski, K.; Smith, D. W. *J. Chromatogr. A* **1997**, *773*, 33.
- (36) Horváth, Cs.; Lin, H.-J. *J. Chromatogr.* **1978**, *149*, 43.
- (37) Gibbs, S. J.; Lightfoot, E. N.; Root, T.W. *J. Phys. Chem.* **1992**, *96*, 7458.
- (38) Knox, J. H.; McLaren, L. *Anal. Chem.* **1964**, *36*, 1477.
- (39) Hawkes, S. J.; Steed, S.P. *J. Chromatogr. Sci.* **1970**, *8*, 256.
- (40) Latour, L. L.; Mitra, P. P.; Kleinberg, R. L.; Sotak, C. H. *J. Magn. Reson. A* **1993**, *101*, 342.
- (41) Knox, J. H.; Scott, H.P. *J. Chromatogr.* **1983**, *282*, 297.
- (42) Epstein, N. *Chem. Eng. Sci.* **1988**, *44*, 777.
- (43) Satterfield, C. N. *Mass Transfer in Heterogeneous Catalysis*; MIT Press: Cambridge, MA, 1970.
- (44) Feng, C.; Stewart, W. E. *Ind. Eng. Chem. Fundam.* **1973**, *12* (2), 143.
- (45) Guan, H.; Guiochon, G.; Coffey, D.; Davis, E.; Gulakowski, K.; Smith, D. W. *J. Chromatogr. A* **1996**, *736*, 21.
- (46) Tallarek, U.; Bayer, E.; van Dusschoten, D.; Van As, H.; Guiochon, G.; Neue, U. D. In Preparation.